PHYSICAL REVIEW C **87**, 045806 (2013)

Measurement of the reaction ^{18}O(α,n)^{21}Ne

A. Best,[1,*] S. Falahat,[1,2] J. Görres,[1] M. Couder,[1] R. deBoer,[1] R. T. Güray,[3] A. Kontos,[1,†] K.-L. Kratz,[2] P. J. LeBlanc,[1,‡] Q. Li,[1]
S. O'Brien,[1,§] N. Özkan,[3] K. Sonnabend,[4] R. Talwar,[1] E. Uberseder,[1] and M. Wiescher[1]
[1]*Department of Physics, University of Notre Dame, Notre Dame, Indiana 46556, USA*
[2]*Department for Biogeochemistry, Max-Planck-Institute for Chemistry, 55020 Mainz, Germany*
[3]*Kocaeli University, Department of Physics, Umuttepe 41380, Kocaeli, Turkey*
[4]*Institute for Applied Physics, Goethe-University Frankfurt, 60325 Frankfurt, Germany*
(Received 2 October 2012; published 29 April 2013)

Background: The reaction ^{18}O(α,n)^{21}Ne is a part of the reaction chains leading to the production of ^{19}F and ^{22}Ne during He burning in low-mass and massive AGB stars, respectively. Additionally, it has been observed as a strong background source in the measurement of other (α,n) reactions.
Purpose: Previously low-energy ^{18}O(α,n)^{21}Ne cross section data have only been available in a non-peer-reviewed form. An improved measurement of this reaction has been done to both clarify its astrophysical influence as well as to provide background yield data for future (α,n) experiments.
Method: The ^{18}O(α,$n_{(0+1)}$) reaction has been measured with a moderating neutron detector. In addition the (α,$n_1\gamma$) channel has been measured independently by observation of the characteristic 350.7 keV γ transition in ^{21}Ne. The reaction cross section at energies above $E_\alpha = 1100$ keV was determined by a simultaneous R-matrix fit to both channels. The strengths of the two lowest-energy resonances at $E_\alpha = 959$ keV and $E_\alpha = 1066$ keV were analyzed separately using individual Breit-Wigner fits.
Results: The cross section of both reaction channels, ^{18}O(α, n_0)^{21}Ne and ^{18}O(α,$n_1\gamma$)^{21}Ne, was determined from the threshold energies at 851 keV and 1280 keV, respectively, to 2300 keV. A new reaction rate has been deduced for the temperature range of 0.1 GK to 10 GK. A previously reported resonance at $E_\alpha = 888$ keV is explained as background from the contaminant reaction ^{17}O(α,n)^{20}Ne.
Conclusions: In general, our reaction rate is slightly lower than the reaction rates in recent compilations. At temperatures below 0.2 GK the present rate is significantly lower because it could be shown that the lowest reported resonance is background from the reaction ^{17}O(α,n)^{20}Ne that has been wrongly assigned to ^{18}O(α,n)^{21}Ne.

DOI: 10.1103/PhysRevC.87.045806 PACS number(s): 26.20.Kn, 24.30.−v, 25.55.−e

I. INTRODUCTION

The reaction ^{18}O(α,n)^{21}Ne with a neutron threshold of $E_\alpha = 851$ keV takes place during He burning at temperatures above $T > 0.3$ GK. It has been proposed as a weak neutron source in the production of ^{19}F in TP-AGB stars [1]. Also, during helium burning in massive stars ^{18}O(α,n)^{21}Ne provides a competing reaction channel to the main reaction chain ^{14}N(α,γ)^{18}F($\beta^+\nu$)^{18}O(α,γ) that synthesizes ^{22}Ne, the main neutron source for the weak s process [2]. The weak s process takes place in two different temperature regimes at different stages of the stellar evolution. The first phase occurs during core He burning at $T \approx 0.3$ GK, the second phase in shell C burning with $T \approx 1$ GK. The (α,γ) reaction is expected to be the dominant reaction channel for temperatures below ≈0.6 GK because of the high reaction threshold of the neutron channel [3,4]. At the most critical, lowest He burning temperatures the stellar reaction rate of the (α,n) channel (e.g., in the NACRE compilation [5]) is based on unpublished cross section measurements with rather large methodological uncertainties [6]. An earlier measurement by Bair and Haas [7] only extends down to stellar burning temperatures >0.6 GK, with an uncertainty of ±25%.

Furthermore, ^{18}O(α,n)^{21}Ne can be a strong background reaction whose contribution has to be carefully subtracted from the experimental measurements of other (α,n) reactions [6,8]. Therefore, a more reliable and accurate knowledge of its reaction cross section down to the threshold is required.

II. EXPERIMENTAL SETUP

The experiment consisted of two independent measurements, a direct measurement of the reaction neutrons and the detection of the characteristic 351 keV γ ray from the ^{18}O(α,$n_1\gamma$)^{21}Ne channel. The specific setups for each part are described separately in the following subsections. Here we describe the parts of the setup that were common to both measurements.

The α beam was provided by the 4MV KN accelerator at the University of Notre Dame Nuclear Science Laboratory. Energy calibration and resolution (1.1 keV) were determined using the well-known $E_p = 991.86 \pm 0.03$ keV and $E_p = 1317.14 \pm 0.07$ keV resonances in ^{27}Al(p, γ)^{28}Si [9]. The beam energy was reproducible within ±2 keV between different hysteresis cycles of the analyzing magnet during the course of the experiment.

---

[*] Present address: Lawrence Berkeley National Laboratory, Berkeley, California 94720, USA; abest1@nd.edu

[†] Present address: National Superconducting Cyclotron Laboratory, Michigan State University, East Lansing, MI 48824, USA.

[‡] Present address: CANBERRA Industries, Inc., Meriden, CT 06450.

[§] Present address: US Government, Washington DC 20009.

Targets were prepared by anodization of 0.3 mm thick tantalum backings using H_2O enriched to 97.2% in ^{18}O.[1] This process is known to produce homogeneous films of Ta_2O_5 [10,11]. The film thickness can be controlled in a reproducible way through regulation of the maximal anodization voltage. Before anodisation the backings were cleaned with acetone and ethanol and then baked out under vacuum for at least 10 min. The target thickness was chosen to be about 9 keV of energy loss for an α beam of 1000 keV for a target orientation of 90° with respect to the beam direction.

To reduce carbon deposition a liquid nitrogen cooled copper tube (cold finger) was mounted in front of the target. A bias of -400 V was applied to the cold finger for suppression of secondary electrons. The beam was rastered with magnetic steerers to produce a beam spot size of 1.4 cm × 1.6 cm on the target. In both parts of the experiment the target chamber was electrically isolated for charge collection and the targets were directly water cooled using deionized water.

The targets were produced using the same settings as in Ref. [12]. The target area density was determined to be $7.5 \times 10^{16}\,\frac{\text{oxygen atoms}}{\text{cm}^2}$ [12] corresponding to an energy loss of $\approx$9 keV at an α energy of 1000 keV.

A. $^{18}\mathrm{O}(\alpha,n_1\gamma)^{21}\mathrm{Ne}$ setup

This part of the experiment was done with two different detectors: The high energy data ($E_\alpha > 1530$ keV) were taken with an unshielded 20% efficiency Ge detector setup. Due to the decrease in yield at lower energies and the natural ^{214}Pb background line at $E_\gamma = 351.9$ keV a Ge detector with higher efficiency (55%) shielded with lead against room background was used to measure the reaction yield down to the n_1 threshold at $E_\alpha = 1280$ keV. In both cases the target was mounted at an angle of 45° with respect to the beam direction.

The high-energy part was done in parallel to the measurement of the $^{17}\mathrm{O}(\alpha,n_1\gamma)^{20}\mathrm{Ne}$ reaction in Ref. [12] and the low-energy data were taken following the $^{17}\mathrm{O}(\alpha,\gamma)^{21}\mathrm{Ne}$ experiment described in Ref. [13]. Both setups were identical to the ones in the respective publications and were used without any reconfiguration in between. Therefore, we only briefly describe the two experimental setups here. More details can be found in the abovementioned references.

The high yield of the $^{18}\mathrm{O}(\alpha,n_1\gamma)^{21}\mathrm{Ne}$ reaction above $E_\alpha =$ 1530 keV allowed us to use an unshielded 20% Ge detector positioned at 45° with respect to the beam. It was placed at a distance of 5.4 cm from the target. In order to minimize radiation damage to the detector crystal a 2.5 cm polyethylene disk was attached to the detector front cap. This significantly reduced the neutron flux in the detector. The transition from the first excited state to the ground state of ^{21}Ne emits a γ ray with an energy of $E_\gamma = 350.7$ keV [9]. Absolute efficiencies were established with calibrated ^{137}Cs, ^{60}Co, and ^{133}Ba sources and augmented using relative efficiency data from ^{56}Co. The resulting efficiency is shown in Fig. 1(a).

The low-energy setup consisted of a 55% efficiency Ge detector positioned at 45° with respect to the beam. To reduce the radiation damage from the strong neutron channel, a polyethylene disk 8.3 cm in diameter and 2.0 cm thick was attached to the front cap of the detector. To optimize efficiency the detector was positioned in close geometry, resulting in a distance of 2.9 cm between target and detector. The target chamber and the detector itself were surrounded by at least 4.5 cm of lead to suppress natural background radiation. Absolute efficiency measurements were done using calibrated sources and the well-known $E_p = 992$ keV resonance in $^{27}\mathrm{Al}(p,\gamma)^{28}\mathrm{Si}$ ($\omega\gamma = 1.93 \pm 0.13$ eV) [14]. The absolute efficiency data were augmented with relative measurements using a ^{56}Co source and the $E_p = 1317$ keV $^{27}\mathrm{Al}(p,\gamma)^{28}\mathrm{Si}$ resonance [15]. The results are shown in Fig. 1(b).

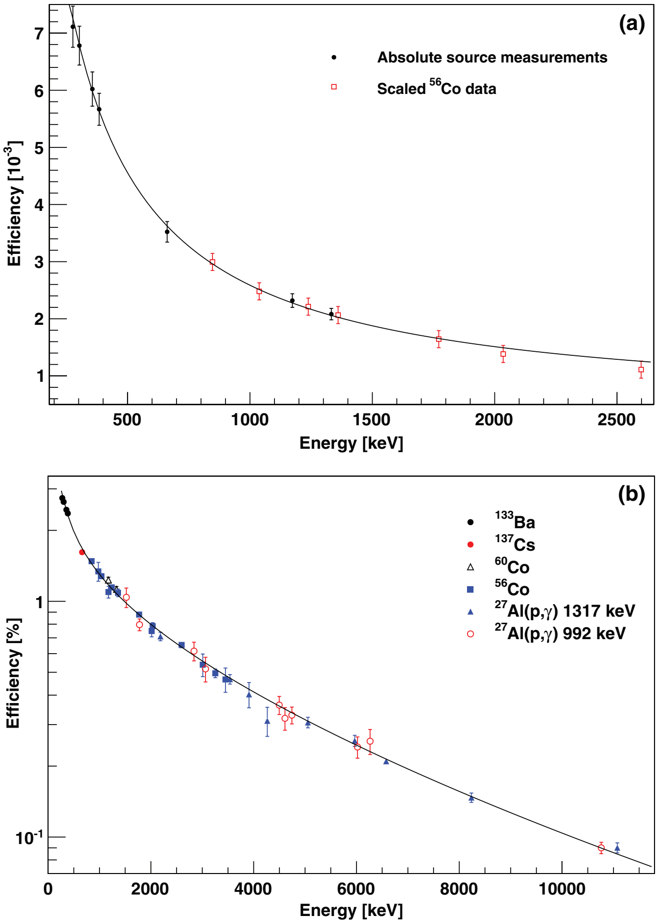

FIG. 1. (Color online) Efficiency of the two Ge detectors. (a) is the smaller detector that was used for the high-energy measurements, (b) is the lead shielded, higher-efficiency setup. The lines are fits to the data points.

B. $^{18}\mathrm{O}(\alpha,\,n_{\mathrm{total}})^{21}\mathrm{Ne}$ setup

The setup used for this part of the experiment has been described in detail in Refs. [12,16]. It is a polyethylene moderated detector using 20 ^{3}He counters arranged in two concentric rings inside the moderator material. A 5 cm shield of borated polyethylene reduces natural neutron background from the outside. The efficiency of the detector has been

---

[1] Purchased from Isotech, Miamisburg, OH. The ^{17}O and ^{16}O contents of the water were 0.6% and 2.2%, respectively.

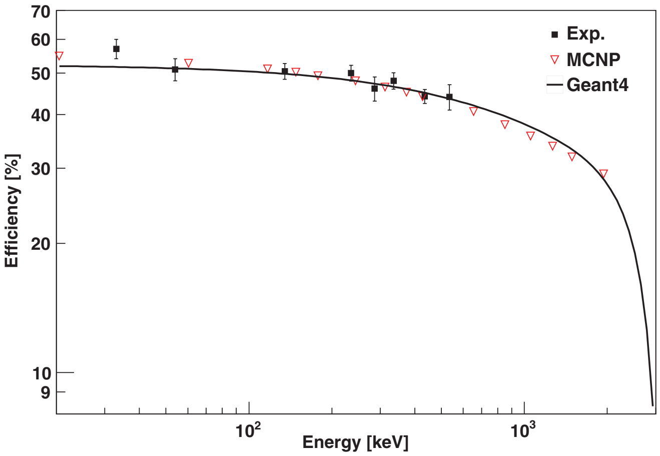

FIG. 2. (Color online) Efficiency of the neutron detector. The black squares are measured efficiencies using the reaction ^{51}V$(p,n)^{51}$Cr. The line and the red triangles are simulation results using GEANT4 and MCNP, respectively. Figure from Ref. [16].

measured with the reaction ^{51}V$(p,n)^{51}$Cr and simulated with the Monte Carlo codes GEANT4 [17] and MNCP [18]. Results of the measurements and the simulations are shown in Fig. 2. For this measurement the target was mounted at an angle of 90° with respect to the beam.

III. EXPERIMENTAL RESULTS

A. ^{18}O(α,$n_1\gamma$)^{21}Ne

An excitation curve of the ^{18}O(α,$n_1\gamma$)^{20}Ne reaction from the n_1 threshold at $E_\alpha = 1280$ keV to 2300 keV was measured in steps of 5 keV or less. For this measurement the $E_\gamma = 350.7$ keV transition from the first excited state to the ground state in the ^{21}Ne nucleus was observed. The yield Y (number of reactions per projectile) was calculated from the intensity I in the 351 keV peak by

$$Y = \frac{I}{Q_{dt}\eta}. \tag{1}$$

Q_{dt} and η represent the dead time corrected number of projectiles and the detector efficiency at 351 keV, respectively. The resulting excitation curve is shown in Fig. 3. The lower-energy part ($E_\alpha < 1530$ keV) of the reaction was measured with the lead shielded, higher-efficiency setup and is shown as red data points in the plot. The measurements with the two setups, the lead shielded 55% HPGe detector and the unshielded 20% setup, overlapped in the energy range of 1520 keV to 1540 keV. Both yields agree within their experimental uncertainties (±6%).

B. ^{18}O(α, $n_{\rm total}$)^{21}Ne

Figure 4 shows the ^{18}O(α,$n_{\rm total}$)^{21}Ne reaction yield that has been measured with the neutron detector described in Sec. II B. The yield was not corrected for the detector efficiency. Above an α energy of 1.28 MeV the population of the first excited state in ^{21}Ne is energetically possible and two neutron groups contribute to the yield. As in our ^{17}O(α,n)^{20}O measurement [12] the occurrence of two neutron groups with different energies makes it necessary to utilize the independent measurement of the (α, $n_1\gamma$) channel to correctly determine the effective neutron energy and with that the detector efficiency.

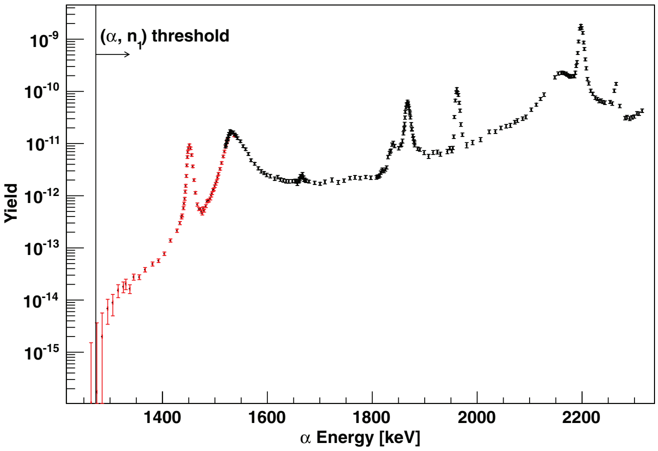

FIG. 3. (Color online) Yield of the ^{18}O(α,$n_1\gamma$)^{21}Ne reaction channel. Red and black data points were taken with the higher- and the lower-efficiency setup, respectively. Also shown is the threshold of the n$_1$ channel at $E_\alpha = 1280$ keV.

Target stability was regularly checked using the $E_\alpha = 1150$ keV resonance and the target was replaced with a fresh one once the yield had degraded. Each color in Fig. 4 corresponds to one of the five targets used during the experiment.

To investigate beam-induced background, mostly dominated by the reaction ^{13}C(α,n)^{16}O with two strong resonances in our region of interest (at $E_\alpha = 1054$ keV and 1336 keV [19]) measurements with a blank Ta target were done covering the full energy range of the experiment. The result of this is also shown in Fig. 4. The two ^{13}C resonances are clearly visible and at the lowest energies the blank target yield is even higher than the yield from our ^{18}O measurements. Both the accumulation of carbon on the targets over time as well as slight changes in the beam tune can have a large impact on the beam-induced background. The analysis of the low-energy

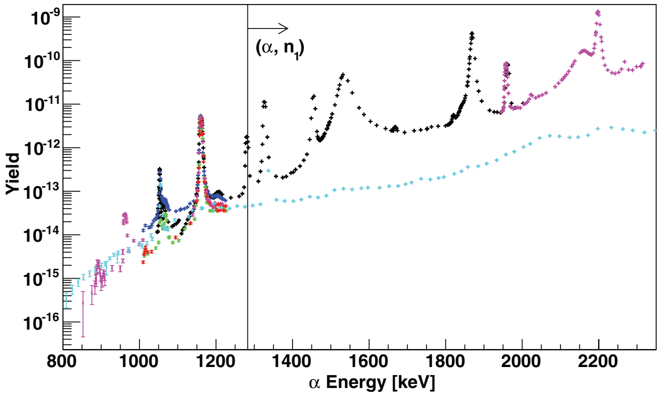

FIG. 4. (Color online) Yield of the ^{18}O(α,$n_{\rm total}$)^{21}Ne reaction. The different colors denote the various targets used over the course of the experiment. The yield from a blank Ta target is shown as the low-lying data points in cyan. Above $E_\alpha = 1280$ keV both the n_0 and n_1 channels are open and contribute to the reaction yield.

part ($E_\alpha < 1100$ keV) of our data will be treated in a separate section (Sec. IV C).

IV. ANALYSIS

A. Separation of the (α,n_0) channel

Because of the occurrence of two neutron groups with different energies above the n_1 threshold at $E_\alpha = 1280$ keV the neutron detector efficiency can only be determined accurately if the branching of the n_0 and n_1 reaction channels is known. Since we independently measured the ^{18}O($\alpha,n_1\gamma$)^{21}Ne reaction by detection of the characteristic $E_\gamma = 350.7$ keV transition its contribution to the ^{18}O(α,n_{total})^{21}Ne reaction could be subtracted from the data. As the target thicknesses used in the two experiments were different due to the different orientation of the target with respect to the beam axis (90° and 45°) we determined the cross section of the ^{18}O($\alpha,n_1\gamma$)^{21}Ne reaction channel with a preliminary R-matrix fit. The simultaneous R-matrix analysis of both channels and the computer code used for the calculations is described in Sec. IV B. All neutron energies involved in the calculations were evaluated at an emission angle of 90 degrees.

As in our previous publication [12] all R-matrix analyses in this work were performed in the framework of a multilevel, multichannel approach based on the formalism outlined for the R-matrix code AZURE [20]. In order to directly fit the R-matrix yield to the measured yield data a target integration routine was added to the program. The standard relationship between cross section and yield was used for this procedure:

$$Y = \int_{E-\Delta E}^{E} \frac{\sigma}{\varepsilon} dE, \tag{2}$$

where Y is the R-matrix yield to be compared to the experimental data, σ is the R-matrix cross section, ε is the stopping power of the target material (Ta_2O_5), and ΔE is the target thickness in terms of energy loss of the projectile. The integration range is a weak function of the beam energy and is calculated at each energy point from the stopping power and the target area density. The fit is a least squares minimization using the experimental data and the calculated yield. Figure 5 shows the results of the preliminary R-matrix fit to the ($\alpha,n_1\gamma$) data. A background pole at $E_x = 11.709$ MeV was included in the fit. The channel radii were set to 5 fm and each target integration was divided into 25 subpoints.

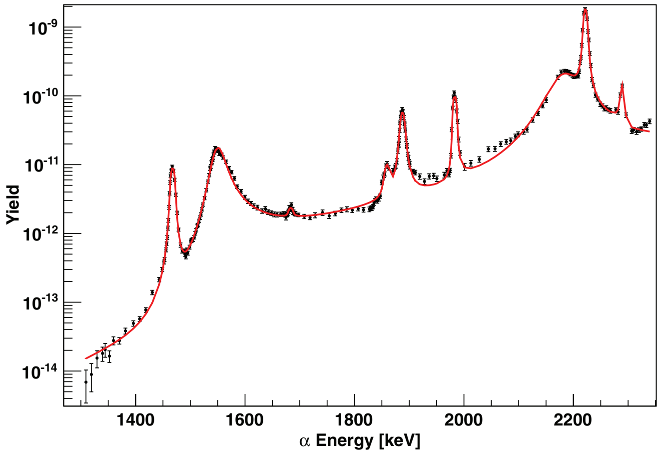

FIG. 5. (Color online) Preliminary R-matrix fit to the ^{18}O($\alpha,n_1\gamma$)^{21}Ne data. The line is the fit to the data points.

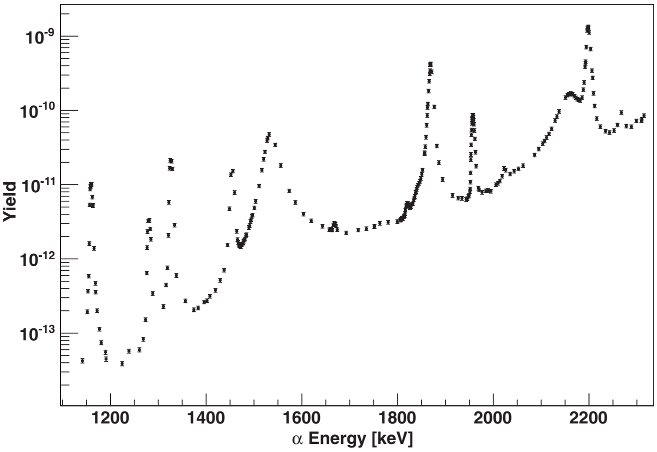

FIG. 6. Yield of the high-energy part of the ^{18}O(α,n_0)^{21}Ne reaction channel that was analyzed using AZURE.

The resulting cross section was integrated using the target thickness of the ^{18}O(α,n_{total})^{21}Ne measurement ($n = 7.5 \times 10^{16} \frac{\text{oxygen atoms}}{\text{cm}^2}$, corresponding to an integration range of about 9 keV) and folded with the detector efficiency (Sec. II B) for the respective neutron energies. The resulting yield was subtracted from the (α,n_{total}) data and the remaining yield was again scaled with the detector efficiency to determine the absolute yield of the ^{18}O(α, n_0)^{21}Ne reaction channel shown in Fig. 6.

B. *R*-matrix calculations

The same background pole ($E_x = 11.709$ MeV) as for the n_1 data was included in the calculation for the (α,n_0) channel. The measured yields and the results of the simultaneous R-matrix fit to both data sets is shown in Fig. 7. To make it easier

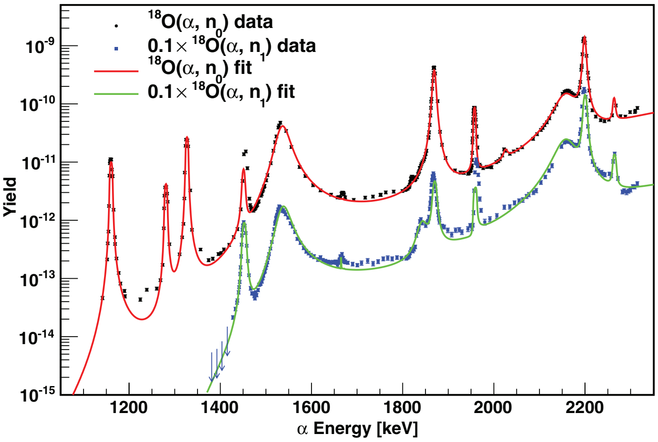

FIG. 7. (Color online) Experimental and calculated yield of the ^{18}O(α,n_0)^{21}Ne and ^{18}O($\alpha,n_1\gamma$)^{21}Ne reaction channels. The lines through the data points are the result of an R-matrix fit to both channels. The n$_1$ channel has been divided by a factor of 10 to better separate it from the n_0 plot. The arrows denote upper limits.

TABLE I. Best-fit R-matrix parameters for the fits shown in Figs. 7 and 8. l and s are the relative angular momentum and the channel spin and Γ is the "observed" partial width as defined in Brune [22]. The "+/−" column shows the relative interference signs needed to reproduce our result. The states are sorted in order of ascending total angular momentum J.

E_x [MeV]	J^π	Channel	l	s	Γ [eV]	+/−	E_x (lit.) [9]
11.709	0^+	α	0	0	3.3×10^3	+	
		n_1	2	2	199×10^3	+	
		n_0	2	2	476×10^3	+	
10.922	1^-	α	1	0	10.5	+	10.922 (3)
		n_1	1	2	6.1×10^3	−	$J^\pi = 1^-$
		n_0	1	1	14.1×10^3	+	$\Gamma = 25(5)$ keV
			1	2	6.6×10^3	+	
11.432	1^-	α	1	0	126	+	11.433 (6)
		n_1	1	2	25.0×10^3	+	$\Gamma = 48$ keV
		n_0	1	1	10.2×10^3	+	
			1	2	5.1×10^3	+	
10.615	2^+	α	2	0	133×10^{-3}	−	10.618 (3)
		n_0	0	2	1.47×10^3	+	$\Gamma = 6$ keV
11.195	2^+	α	2	0	13.8	+	11.195 (3)
		n_1	0	2	440	−	$J \leqslant 5$
		n_0	0	2	4.8×10^3	+	$\Gamma = 7$ keV
11.518	2^+	α	2	0	4.6	+	11.520 (15)
		n_1	0	2	1.6×10^3	+	$\Gamma = 6$ keV
		n_0	0	2	1.5×10^3	+	
10.713	3^-	α	3	0	44.5×10^{-3}	+	10.706 (6)
		n_0	1	2	1.7×10^3	+	$1 \leqslant J \leqslant 6$
							$\Gamma < 10$ keV
10.853	3^-	α	3	0	224×10^{-3}	+	10.858 (3)
		n_1	1	2	1.9×10^3	+	$1 \leqslant J \leqslant 4$
			1	3	45.8	+	$\Gamma = 6$ keV
		n_0	1	2	1.7×10^3	+	
11.172	3^-	α	3	0	359×10^{-3}	−	11.161 (15)
		n_1	1	2	19.3×10^3	+	
			1	3	476	+	
11.268	3^-	α	3	0	1.6	+	11.271 (4)
		n_1	1	2	412	+	$2 \leqslant J \leqslant 4$
			1	3	10.2	+	$\Gamma = 12$ keV
		n_0	1	2	1.2×10^3	−	
10.751	4^+	α	4	0	225×10^{-3}	+	10.751 (3)
		n_0	2	2	1.6×10^3	+	$J^\pi = 5^-$
							$\Gamma = 6$ keV
11.465	4^+	α	4	0	49.9	−	11.465 (3)
		n_1	2	2	1.0×10^3	+	$\Gamma < 3$ keV
			2	3	1.0×10^3	+	
		n_0	2	2	2.5×10^3	+	
11.323	5^-	α	5	0	98×10^{-3}	+	
		n_0	3	2	7.4×10^3	+	
11.03	6^+	α	6	0	1.4×10^{-3}	+	11.032 (6)
		n_1	4	3	9.3	+	$\Gamma < 10$ keV
		n_0	4	2	9.0	+	

to distinguish between the two channels the n_1 plot has been scaled down by a factor of 10. The best-fit R-matrix parameters from our calculation are shown in Table I. The relationship between the "observed" partial widths Γ and R matrix reduced widths γ (as defined in Ref. [21]) is $\Gamma_{ic} = \frac{2P_c\gamma_{ic}^2}{1+\sum_c \gamma_{ic}^2 (\frac{dS_c}{dE})_{E_i}}$ [22], where P_C and S_C are the penetration and the shift factor. It was not possible to reproduce the strength of the $E_\alpha = 1083$ keV ($E_x = 10.751$ MeV) resonance using the spin-parity of $J^\pi = 5^-$ (requiring an α orbital momentum of $l = 5$) from Ref. [9].

The uncertainty in the absolute scale of the cross section is mostly influenced by the efficiency determination of the neutron and the γ-ray detectors and by the target thickness that is used in the integration process. R-matrix fits for various thicknesses were performed and the effect on the calculated cross section was determined to be ±10%.

Following additional systematic uncertainties have to be attributed to the data: The error in the (α,n_1) s factor was calculated by quadratic addition of the ±10% from the target thickness and the ±6% of the measurement to ±12%. The uncertainty in the lower-energy (α,n_0) data between the n_1 threshold and the lowest resonance included in the R-matrix fit (1.1 MeV $< E_\alpha <$ 1.28 MeV) is ±11% (10% target thickness and 5.5% detector efficiency). Finally, since the n_0 data above the n_1 threshold is the result of a combination of both γ and neutron measurements the associated error is the quadratic addition of both uncertainties, or ±16%.

To give a direct comparison with the data we also converted our experimental yield into cross section by a least-squares deconvolution method based on the description in Ref. [23]: in short, yield data were calculated by the integration of the cross section over the target thickness. The starting point was the cross section obtained from the R-matrix fit, which was then varied until the new integrated cross section agreed with the experimental yield. The results, where the cross section has been converted into the astrophysical S-factor $S(E) = E\sigma(E)e^{-2\pi\eta}$ is shown in Fig. 8. η stands for the Sommerfeld parameter.

C. Low-energy resonances

The three lowest-energy, narrow resonances (at $E_\alpha =$ 888 keV, $E_\alpha = 959$ keV, and $E_\alpha = 1066$ keV, not shown in

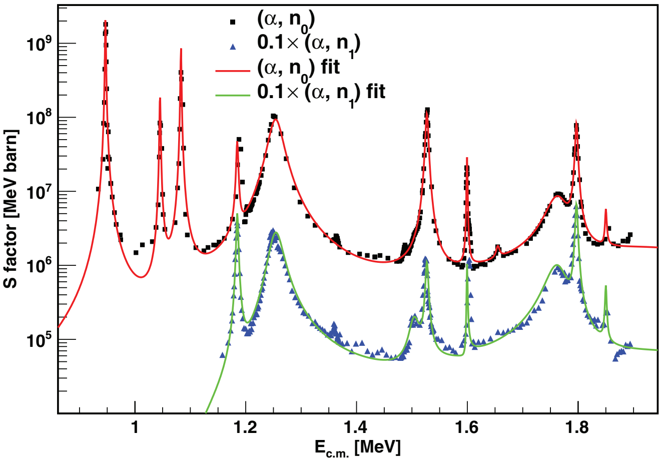

FIG. 8. (Color online) Astrophysical S factor of the ^{18}O(α,n_0)^{21}Ne and ^{18}O(α,$n_1\gamma$)^{21}Ne reaction channels. Shown as the points is the S factor that was directly extracted from the experimental data (see text) for both channels. The respective R-matrix S factors are represented by lines. The data of the (α,$n_1\gamma$) channel were multiplied by a factor of 0.1 to better visually separate the plots.

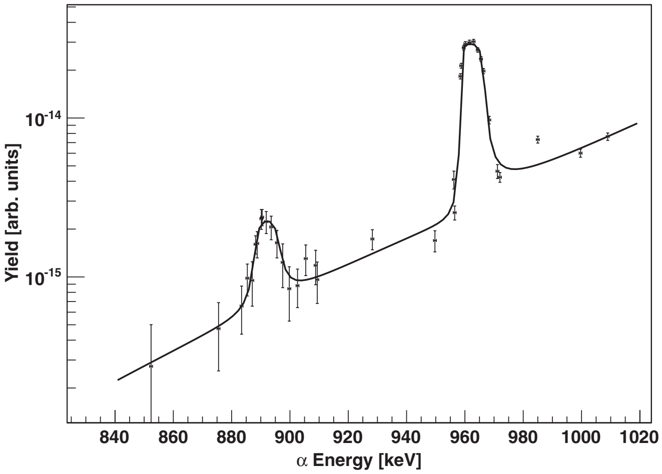

FIG. 9. Neutron yield (not efficiency corrected) in the energy region around the $E_\alpha = 888$ keV and 959 keV resonances. The line through the data points is a fit using Eq. (3).

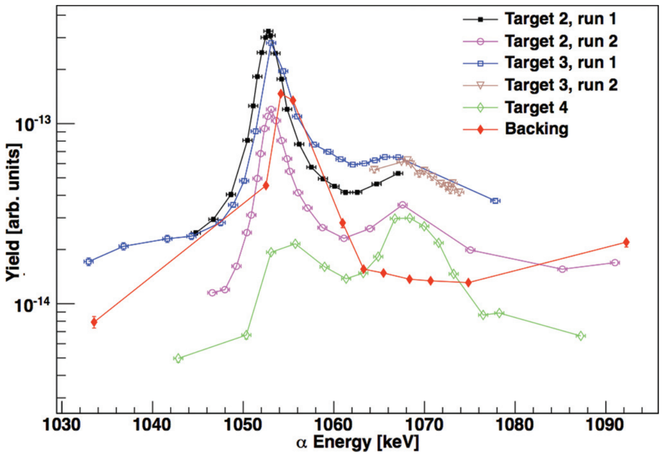

FIG. 10. (Color online) Yield around the $E_\alpha = 1066$ keV resonance in ^{18}O(α,n). The different markers and colors denote measurements using different targets and different experimental runs using the same target. The $E_\alpha = 1054$ keV resonance in ^{13}C(α,n) has a dramatic influence on the yield in the surrounding energy region. The full diamonds in red are blank target data. The lines through the data points are to guide the eye.

the above figures of the R-matrix results) would be difficult to include into the R-matrix calculation. The large background resulting from the ^{13}C(α,n)^{16}O reaction on carbon deposition on the target dominates the observed yield between the resonances. Therefore, the strengths of these resonances were evaluated separately. Figure 9 shows the yield (not efficiency corrected) of the $E_\alpha = 888$ keV and 959 keV resonances and a fit to the data. The fit function consisted of an exponential background that can be attributed to ^{13}C(α,n)^{16}O and two Breit-Wigner functions that were integrated over the target thickness Δ (in terms of energy loss of the projectile):

$$\begin{aligned} Y(E) = e^{(c_0+c_1E)} &+ c_2\left(\arctan\left(\frac{E-E_{R,1}}{\frac{\Gamma_{1,a}}{2}}\right)\right. \\ &\left.- \arctan\left(\frac{E-E_{R,1}-\Delta}{\frac{\Gamma_{1,b}}{2}}\right)\right) \\ &+ c_3\left(\arctan\left(\frac{E-E_{R,2}}{\frac{\Gamma_{2,a}}{2}}\right)\right. \\ &\left.- \arctan\left(\frac{E-E_{R,2}-\Delta}{\frac{\Gamma_{2,b}}{2}}\right)\right). \end{aligned} \tag{3}$$

E_R and Γ are the resonance energies and the resonance widths. To simulate the broadening of the high-energy flank of the resonances due to straggling effects two different widths $\Gamma_{a,b}$ were included. The target thickness varies with energy, but since the two resonances lie very close to each other no significant error is introduced by keeping the same Δ for both cases. The constants c_2 and c_3 include the resonance strength $\omega\gamma$:

$$c = \eta\frac{\lambda_r^2}{2\pi}\frac{\omega\gamma}{\epsilon_r}. \tag{4}$$

The deBroglie wavelength λ and the stopping power ϵ are in the center-of-mass system. The detector efficiency is expressed through η.

A resonance at $E_\alpha = 888$ keV has also been observed in the ^{17}O(α,n)^{20}Ne reaction (see Ref. [12]). The yield of the resonance in $^{17}\text{O}+\alpha$ is two orders of magnitude higher than the yield seen in this experiment. According to the supplier the water that was used to produce the ^{18}O targets contains 0.6% of ^{17}O and the enrichment in ^{17}O in Ref. [12] is 90.1%. Scaling the observed strength correspondingly the observation of the 888 keV resonance can be fully assigned to the contribution from the small contamination with ^{17}O in the enriched water.

The results of the fit and the extracted parameters for the 959 keV resonance are given in Table II. The 11-parameter fit has a reduced χ^2 of $\frac{69}{26} = 2.65$. Besides the error in c from the fit an uncertainty of ±5% in the stopping power and ±5.4% in the efficiency of the neutron detector were taken into account. The statistical uncertainty and the error in the determination of the deposited charge were included in the yield points and directly propagated into the fit.

An additional complication arises in the case of the $E_\alpha = 1066$ keV resonance: it lies next to the strong $E_\alpha = 1054$ keV resonance in ^{13}C(α,n)^{16}O [19]. Figure 10 shows the yield in this energy region. Measurements at this resonance were

TABLE II. Low-energy ^{18}O(α,n)^{21}Ne resonance parameters. $E_{\alpha,D}$ and $\omega\gamma_D$ are the resonance parameters reported in Ref. [6].

E_α [keV]	E_R [keV]	E_x [keV]	c [10^{-16}]	η	$\epsilon_r[\frac{\text{eVcm}^2}{\text{atom}}]$	$\omega\gamma$ [meV]	$E_{\alpha,D}$ [keV]	$\omega\gamma_D$ [meV]
958.6 (3)	784.3 (2)	10452	93 ± 4	0.51	9.15×10^{-14}	2.67 (23)	946 (4)	2.88 (24)
1065.6 (9)	871.4 (7)	10540	9.96 ± 3.09	0.5	9.05×10^{-14}	3.2 (10)	1057 (3)	3.2 (3)

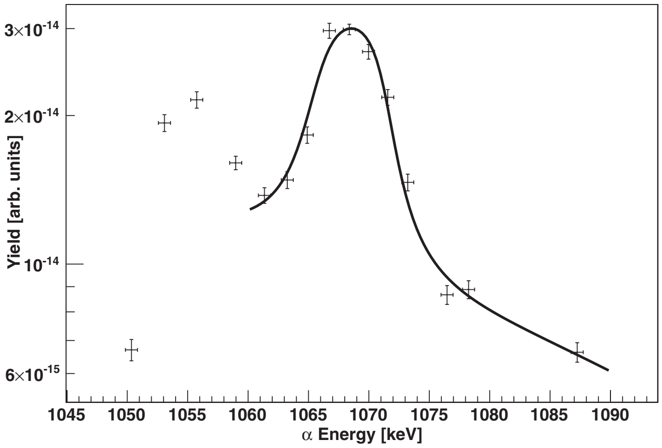

FIG. 11. Thick-target Breit-Wigner fit to the $E_\alpha = 1066$ keV resonance. The data points are from the measurements done with target 4 that showed the lowest beam-induced background contribution.

done using three different targets to determine the carbon contamination. The different runs are denoted by the different markers and colors. The large variation in the beam-induced background is clearly visible, and one of the measurements (target 4) shows a relatively low ^{13}C(α,n) yield.

The resonance strength was determined from the low-background data measured with target 4 (the lowest-lying data points marked by green open diamonds in Fig. 10) in a similar way as for the lower-energy resonances above. The following integrated Breit-Wigner function situated on a linear background was fit to the yield data:

$$Y(E) = c_0 + c_1 E + c_2\left(\arctan\left(\frac{E - E_R}{\frac{\Gamma_a}{2}}\right) - \arctan\left(\frac{E - E_R - \Delta}{\frac{\Gamma_b}{2}}\right)\right). \quad (5)$$

The results of the fit ($\chi^2 = \frac{7.35}{4} = 1.84$) and the calculated resonance parameters are shown in Fig. 11 and Table II.

As stated in the Introduction, unpublished results from a Ph.D. thesis by Denker [6] have been incorporated into the NACRE reaction rate compilation [5]. The resonances described here were also seen in that work. For comparison the strengths reported by Denker are also shown in Table II.

Denker subtracted an ^{18}O contribution from their ^{17}O measurement, but in Ref. [6] they do not state the isotopic mixture of the target gas that was used in the ^{18}O measurement and do not mention a possible contribution from ^{17}O(α, n)^{20}Ne as a background source in their ^{18}O data. Therefore, the lowest-energy resonance in their work is most likely spuriously assigned to the reaction ^{18}O(α, n)^{21}Ne and should not be included in the calculation of the reaction rate.

V. ASTROPHYSICAL REACTION RATE

The rate of the ^{18}O(α,n)^{21}Ne reaction was calculated in the temperature range of 0.1 to 10 GK. For temperatures above 2 GK reaction rates were calculated with the Hauser-Feshbach code CIGAR [24] and normalized to our experimental results at $T = 2$ GK.

The reaction rate (in units of cm^3 mol^{-1} s^{-1}) was calculated by numerical integration of the R-matrix cross section $\sigma(E)$ (in barns) using the expression [25]

$$N_A\langle\sigma v\rangle_{01} = \frac{3.7318\times 10^{10}}{T^{3/2}}\sqrt{\frac{M_0 + M_1}{M_0 M_1}} \cdot \int_0^\infty E\sigma(E)e^{-11.605E/T}dE\ . \quad (6)$$

The contribution to the rate from the two low-energy resonances at $E_\alpha = 959$ and $E_\alpha = 1066$ keV was calculated from the values in Table II using the equation for isolated, narrow resonances and then added to the R-matrix rate:

$$N_A\langle\sigma v\rangle = \frac{1.5399\times 10^{11}}{\left(\frac{M_0 M_1}{M_0+M_1}T\right)^{3/2}}\sum_i(\omega\gamma)_i e^{-11.605E/T}. \quad (7)$$

TABLE III. Rate of the ^{18}O(α, n)^{21}Ne reaction (in units of cm^3 mol^{-1} s^{-1}). Above $T = 2$ GK the extrapolated rates are Hauser-Feshbach calculations.

T [GK]	$N_A\langle\sigma v\rangle$ (lower)	$N_A\langle\sigma v\rangle$ (recomm.)	$N_A\langle\sigma v\rangle$ (upper)
0.1	7.90×10^{-37}	9.16×10^{-37}	1.04×10^{-36}
0.11	2.34×10^{-33}	2.70×10^{-33}	3.06×10^{-33}
0.12	1.91×10^{-30}	2.19×10^{-30}	2.47×10^{-30}
0.13	5.63×10^{-28}	6.43×10^{-28}	7.23×10^{-28}
0.14	7.38×10^{-26}	8.39×10^{-26}	9.39×10^{-26}
0.15	5.04×10^{-24}	5.70×10^{-24}	6.37×10^{-24}
0.16	2.02×10^{-22}	2.28×10^{-22}	2.54×10^{-22}
0.17	5.25×10^{-21}	5.90×10^{-21}	6.56×10^{-21}
0.18	9.46×10^{-20}	1.06×10^{-19}	1.17×10^{-19}
0.2	1.28×10^{-17}	1.43×10^{-17}	1.59×10^{-17}
0.25	9.21×10^{-14}	1.02×10^{-13}	1.13×10^{-13}
0.3	3.92×10^{-11}	4.40×10^{-11}	4.88×10^{-11}
0.35	3.50×10^{-9}	3.95×10^{-9}	4.40×10^{-9}
0.4	1.14×10^{-7}	1.29×10^{-7}	1.44×10^{-7}
0.45	1.84×10^{-6}	2.09×10^{-6}	2.34×10^{-6}
0.5	1.77×10^{-5}	2.01×10^{-5}	2.25×10^{-5}
0.6	5.68×10^{-4}	6.46×10^{-4}	7.25×10^{-4}
0.7	7.25×10^{-3}	8.25×10^{-3}	9.24×10^{-3}
0.8	5.16×10^{-2}	5.87×10^{-2}	6.58×10^{-2}
0.9	2.48×10^{-1}	2.82×10^{-1}	3.17×10^{-1}
1.0	9.07×10^{-1}	1.03×10^{0}	1.15×10^{0}
1.25	1.05×10^{1}	1.19×10^{1}	1.34×10^{1}
1.5	6.15×10^{1}	6.99×10^{1}	7.83×10^{1}
1.75	2.36×10^{2}	2.68×10^{2}	3.01×10^{2}
2.0	6.83×10^{2}	7.77×10^{2}	8.70×10^{2}
2.5	4.49×10^{3}	5.11×10^{3}	5.72×10^{3}
3.0	1.78×10^{4}	2.02×10^{4}	2.27×10^{4}
3.5	5.13×10^{4}	5.83×10^{4}	6.53×10^{4}
4.0	1.19×10^{5}	1.35×10^{5}	1.51×10^{5}
5.0	4.21×10^{5}	4.79×10^{5}	5.36×10^{5}
6.0	1.04×10^{6}	1.18×10^{6}	1.32×10^{6}
7.0	2.05×10^{6}	2.34×10^{6}	2.62×10^{6}
8.0	3.52×10^{6}	4.01×10^{6}	4.49×10^{6}
9.0	5.44×10^{6}	6.19×10^{6}	6.94×10^{6}
10.0	7.82×10^{6}	8.89×10^{6}	9.96×10^{6}

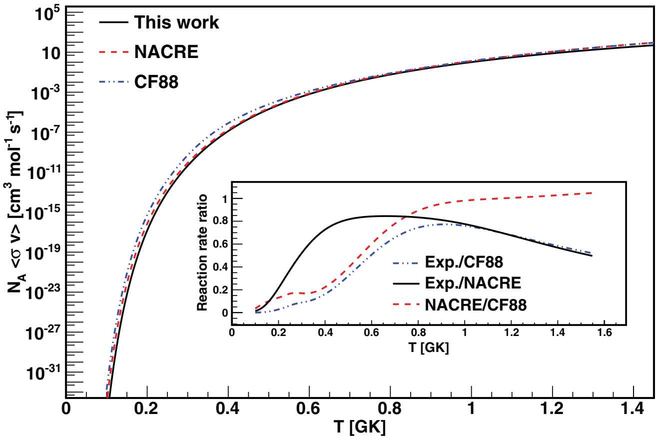

FIG. 12. (Color online) Reaction rate of the ^{18}O(α,n)^{21}Ne reaction. Shown in black is the rate from the current experiment, the red dashed line and the blue dash-dotted lines represent the NACRE [5] and the CF88 [26] rates, respectively. The inset displays the ratios between the different rates.

In both cases M_0 and M_1 stand for the masses of the reaction partners in atomic mass units, the temperature T is given in GK and the c.m. energy E in MeV. The recommended and $\pm 1\sigma$ reaction rates are listed in Table III. The values in the columns denoted by (lower) and (upper) were calculated using the uncertainty in the R-matrix cross section ($\pm 12\%$) and the error in the resonance strengths and energies of the two low-energy resonances. A comparison with the available literature rates in the relevant temperature range (NACRE [5] and CF88 [26]) is shown in Fig. 12. The insets show the ratio of the respective rates with the literature rates from CF88. The stronger deviation from NACRE at low temperatures can be attributed to their inclusion of the $E_\alpha = 888$ keV resonance that we assign to the ^{17}O(α,n)^{20}Ne reaction.

VI. SUMMARY

We have measured the ^{18}O(α,n)^{21}Ne reaction cross section from the neutron threshold at $E_\alpha = 851$ keV to 2300 keV at the Notre Dame Nuclear Science Laboratory. A previously reported resonance at $E_\alpha = 888$ keV [6] is explained as due to beam-induced background on contaminant ^{17}O in the target.

A reaction rate from $T = 0.1$ GK to 10 GK has been calculated. Our rate is $\approx$20%–30% percent lower than the NACRE rate, except at the very lowest temperatures, where we excluded the contribution from the spurious 888 keV resonance.

ACKNOWLEDGMENTS

The authors express their gratitude to the technical staff of the Nuclear Science Laboratory at Notre Dame. This work was funded by the National Science Foundation through Grant No. Phys-0758100 and the Joint Institute for Nuclear Astrophysics supported through the NSF Physics Frontier Center program, Grant No. Phys-0822648.

---

[1] A. Jorissen, V. V. Smith, and D. L. Lambert, Astron. Astrophys. **261**, 164 (1992).
[2] F. Käppeler, R. Gallino, S. Bisterzo, and W. Aoki, Rev. Mod. Phys. **83**, 157 (2011).
[3] H.-P. Trautvetter, M. Wiescher, K. Kettner, C. Rolfs, and J. Hammer, Nucl. Phys. A **297**, 489 (1978).
[4] S. Dababneh, M. Heil, F. Käppeler, J. Görres, M. Wiescher, R. Reifarth, and H. Leiste, Phys. Rev. C **68**, 025801 (2003).
[5] C. Angulo, M. Arnould, M. Rayet, P. Descouvemont, D. Baye, C. Leclercq-Willain, A. Coc, S. Barhoumi, P. Aguer, C. Rolfs *et al.*, Nucl. Phys. A **656**, 3 (1999).
[6] A. Denker, Ph.D. thesis, Universität Stuttgart, 1994.
[7] J. Bair and F. Haas, Phys. Rev. C **7**, 1356 (1973).
[8] S. Falahat, Ph.D. thesis, Max-Planck Institut für Chemie Mainz, 2010.
[9] P. Endt, Nucl. Phys. A **521**, 1 (1990).
[10] D. Vermilyea, Acta Metall. **1**, 282 (1953).
[11] M. Seah, M. Holbourn, C. Ortega, and J. Davies, Nucl. Instrum. Methods Phys. Res. B **30**, 128 (1988).
[12] A. Best, M. Beard, J. Görres, M. Couder, R. deBoer, S. Falahat, R. Güray, A. Kontos, K.-L. Kratz, P. LeBlanc *et al.*, Phys. Rev. C **87**, 045805 (2013).
[13] A. Best, J. Görres, M. Couder, R. deBoer, S. Falahat, A. Kontos, P. J. LeBlanc, Q. Li, S. O'Brien, K. Sonnabend *et al.*, Phys. Rev. C **83**, 052802(R) (2011).
[14] B. Paine and D. Sargood, Nucl. Phys. A **331**, 389 (1979).
[15] P. M. Endt, C. Alderliesten, F. Zijderhand, A. A. Wolters, and A. G. M. van Hees, Nucl. Phys. A **510**, 209 (1990).
[16] S. Falahat, A. Best, M. Couder, J. Görres, K.-L. Kratz, U. Ott, E. Stech, and M. Wiescher, Nucl. Instrum. Methods Phys. Res. A **700**, 53 (2013).
[17] S. Agostinelli *et al.*, Nucl. Instrum. Methods Phys. Res. A **506**, 250 (2003).
[18] X-5 Monte Carlo Team (2003), Los Alamos National Laboratory, MCNP - A general Monte Carlo N-Particle Transport Code - version 5, https://laws.lanl.gov/vhosts/mcnp.lanl.gov/.
[19] S. Harissopulos, H. W. Becker, J. W. Hammer, A. Lagoyannis, C. Rolfs, and F. Strieder, Phys. Rev. C **72**, 062801(R) (2005).
[20] R. Azuma, E. Uberseder, E. Simpson, C. Brune, H. Costantini, R. de Boer, J. Görres, M. Heil, P. LeBlanc, C. Ugalde *et al.*, Phys. Rev. C **81**, 045805 (2010).
[21] A. Lane and R. Thomas, Rev. Mod. Phys. **30**, 257 (1958).
[22] C. R. Brune, Phys. Rev. C **66**, 044611 (2002).
[23] V. A. McGlone and P. B. Johnson, Nucl. Instrum. Methods Phys. Res. B **61**, 201 (1991).
[24] R. Crowter, Master's thesis, University of Surrey, 2008.
[25] W. A. Fowler, G. R. Caughlan, and B. A. Zimmermann, Annu. Rev. Astron. Astrophys. **13**, 69 (1975).
[26] G. Caughlan and W. Fowler, At. Data Nucl. Data Tables **40**, 283 (1988).